PAPER

Check for updates

Highly efficient removal of dibutyl phthalate from wastewater using a novel hydrophilic–lipophilic magnetic adsorbent based on silica-coated iron oxide nanoparticles†

Sarah Alharthi, [ab] Tahira Bibi,[c] Eman Y. Santali[d] and Ashraf Ali *[e]

The widespread occurrence of dibutyl phthalate (DBP) in aquatic systems demands effective remediation approaches. This study developed a novel magnetic adsorbent ($Fe_3O_4@SiO_2$-R) through the surface functionalization of silica-coated iron oxide nanoparticles with octadecyl silane and (3-aminopropyl) trimethoxy silane (APTMS) to incorporate both hydrophobic and hydrophilic groups. Comprehensive characterization (SEM, XRD, FTIR, XPS) confirmed the successful synthesis of the adsorbent. Batch adsorption experiments systematically evaluated the DBP removal across different water matrices (river water, municipal and industrial wastewater), examining the effect of concentration, contact time, adsorbent dose, and pH effects. The adsorbent demonstrated exceptional performance with a maximum adsorption capacity of 645.43 mg g^{-1} and removal efficiencies of 98.4%, 94.2%, and 88.7% in the respective matrices, reducing DBP to <6 µg L^{-1}. The process simultaneously decreased the total organic content (TOC) by 18% and chemical oxygen demand (COD) by 22%, indicating effective co-removal of the organic pollutants. Adsorption followed the Langmuir isotherm ($R^2 = 0.994$) and pseudo-second-order kinetics, suggesting monolayer chemisorption. Remarkably, after 30 reuse cycles, the removal efficiency decreased by only 20%, demonstrating excellent reusability. Comparative analysis revealed that the adsorbent outperformed many existing materials in terms of adsorption capacity and operational simplicity. These findings highlight $Fe_3O_4@SiO_2$-R as an efficient adsorbent for plasticizer removal, with significant potential for practical water treatment applications while supporting SDG targets for clean water.

1 Introduction

Phthalic acid esters (PAEs) are a class of endocrine-disrupting chemicals that pose significant risks to human and animal health.[1] PAEs are widely used as plasticizers in polyvinyl chloride (PVC) to improve the flexibility and durability of plastics, making them essential in numerous consumer and industrial applications. However, because PAEs are not chemically bound to the polymer matrix, they can leach out over time, contaminating food, beverages, and the surrounding environment.[2]

[a]Department of Chemistry, College of Science, Taif University, Taif 21944, Saudi Arabia

[b]Research Center of Basic Sciences, Engineering and High Altitude, Taif University, Taif 21944, Saudi Arabia

[c]Department of Chemistry, Faculty of Physical & Applied Sciences, The University of Haripur, Haripur 22620, Pakistan

[d]Department of Pharmaceutical Chemistry, College of Pharmacy, Taif University, Taif, 21944, Saudi Arabia

[e]School of Chemistry & Chemical Engineering, Henan University of Technology, Zhengzhou 450000, China

† Electronic supplementary information (ESI) available. See DOI: https://doi.org/10.1039/d5na00436e

Beyond plastics, PAEs are also found in adhesives, sealants, paints, surface coatings, and even cosmetics, further increasing human exposure.[3–5] The extensive use of PAEs has raised serious environmental and public health concerns due to their well-documented toxic effects. Studies have linked PAE exposure to reproductive toxicity, neurotoxicity, metabolic disorders, carcinogenicity, and genotoxicity.[6] Some phthalates have been classified as potential carcinogens, particularly due to their harmful effects on the male reproductive system.[7] Aquatic environments are especially at risk, with reported PAE concentrations in water sources ranging from 3 to 70 µg L^{-1}.[5,8,9] Their persistence is evident in their widespread detection in groundwater, surface water, and soil, posing long-term ecological and health hazards.[10] Given their toxicity, bioaccumulation potential, and environmental persistence, six major phthalates have been listed as priority pollutants by the U.S. Environmental Protection Agency (EPA).[7] As a result, there is an urgent need for effective remediation strategies to mitigate PAE contamination and protect both ecosystem health and human well-being. Dibutyl phthalate (DBP) is widely used as a plasticizer and solvent in personal care products (e.g., nail polishes, perfumes, and hairsprays) to enhance flexibility and fragrance longevity.[11]

However, its health risks are well-documented, including ocular irritation (photophobia, conjunctivitis), systemic toxicity, and dermatological effects.[12] Toxicological studies in rats reported an oral LD_{50} of 8–10 g kg^{-1} and an intraperitoneal LD_{50} of ~4 g kg^{-1}, indicating moderate acute toxicity. In humans, exposure *via* inhalation, dermal contact, or ingestion can cause burning sensations, dizziness, nausea, and contact dermatitis.[13] Due to these risks, regulatory agencies have imposed strict limits: the U.S. EPA classifies DBP as a priority pollutant with a maximum contaminant level (MCL) of 6 µg L^{-1} in drinking water, while the EU's Water Framework Directive lists it as a 'priority hazardous substance' with an annual average limit of 1.3 µg L^{-1} for inland waters. Despite these regulations, DBP levels in wastewater and surface waters (*e.g.*, 3–70 µg L^{-1} in Asian rivers) often exceed thresholds due to plastic leaching and inefficient conventional treatments. This gap underscores the need for advanced adsorbents capable of reducing DBP to sub-µg L^{-1} levels, as demonstrated in this study.

Numerous methods have been used for the removal of phthalates from water, such as advanced oxidation process,[14] coagulation,[15] ion-exchange method,[16] photocatalytic degradation,[17] bioremediation,[18,19] and adsorption.[20,21] Adsorption has several advantages over other techniques, including high efficiency, sludge-free operation, and low energy requirements.[22,23] Conventional adsorbents like activated carbon,[24] clay minerals,[25] polymeric resins, cellulose-based adsorbents[26] and biosorbent[27] have been commonly employed for PAE removal; however, these materials face significant limitations that restrict their practical application. Their insufficient adsorption sites, low extraction efficiency, poor selectivity in complex matrices, and challenging regeneration processes often result in suboptimal performance. These shortcomings highlight the critical need for developing advanced adsorbents with enhanced properties for effective PAE remediation. Recent research has focused on engineered materials featuring high-density functional groups, tailored porosity, and improved surface chemistry to overcome these limitations.[28,29] Novel approaches incorporating magnetic components, molecular imprinting technology, and hybrid nanocomposites show promise, offering superior adsorption capacity, selective recognition, and easier recovery compared to traditional adsorbents.[30–32] The development of advanced adsorbent could provide more efficient, cost-effective, and sustainable solutions for addressing pollutant contamination in water systems.[33–38]

Recent advances in the adsorbent design for PAE removal have employed molecular imprinting and surface modification techniques to enhance selectivity.[39] Yang *et al.*[40] developed yolk–shell magnetic mesoporous carbon MIPs with excellent adsorption for dioctyl phthalate. However, MIPs face challenges including templating molecule removal difficulties during preparation, high organic solvent consumption, and demanding cleaning requirements, limiting their practical application. Recent studies have highlighted surface modification as an effective strategy to enhance adsorption sites and selectivity for PAE removal.[25,41] Fan *et al.* reported improved dibutyl phthalate adsorption (27.4 mg g^{-1}) using phenyl-modified SBA-15, although the adsorption was limited by poor

water dispersibility.[25] Polar groups are incorporated into hydrophobic adsorbents to improve their dispersibility in aqueous medium. Such adsorbents are termed as amphiphilic adsorbents, which have shown superior performance to hydrophobic and hydrophilic adsorbents for PAEs removal but face complex synthesis and recovery challenges.[28,42]

Despite significant progress in adsorbent development for phthalate (PAE) removal, critical limitations persist in the current technologies. While molecularly imprinted polymers (MIPs) offer selectivity, their practical application is hindered by complex synthesis, high solvent consumption, and templating molecule removal challenges.[40] Surface-modified adsorbents, such as phenyl-functionalized SBA-15, improve adsorption capacity but suffer from poor aqueous dispersibility.[25] Additionally, conventional adsorbents like activated carbon and clay minerals exhibit insufficient adsorption sites, low selectivity, and regeneration issues, limiting their efficiency in real-world water treatment scenarios.[24,25,27] There remains a pressing need for adsorbents that combine ease of synthesis, high adsorption capacity, selectivity, magnetic separability, and reusability features not simultaneously addressed in existing solutions. Our work bridges this gap by developing a one-step synthesized amphiphilic magnetic adsorbent that integrates hydrophobic alkyl chains and hydrophilic amino groups on a silica-coated Fe_3O_4 core, enabling efficient DBP removal through synergistic hydrophobic and hydrogen-bonding interactions while permitting rapid magnetic recovery. This design overcomes the trade-offs between performance, practicality, and cost-effectiveness observed in current systems, offering a scalable solution for PAE remediation.

The present study introduces a novel amphiphilic magnetic adsorbent, $Fe_3O_4@SiO_2$-R, which uniquely combines hydrophobic octadecyl silane (C18) and hydrophilic (3-aminopropyl) trimethoxy silane (APTMS) functional groups on a silica-coated iron oxide core in a single-step synthesis. This design addresses critical limitations of existing adsorbents by integrating three key innovations including dual-functionality, magnetic separability and facile synthesis. The simultaneous presence of hydrophobic alkyl chains and hydrophilic amino groups enables synergistic interactions with dibutyl phthalate (DBP) through hydrophobic partitioning, hydrogen bonding, and electrostatic forces, significantly enhancing adsorption capacity and selectivity. The Fe_3O_4 core allows rapid recovery using an external magnetic field, overcoming the separation challenges faced by conventional amphiphilic adsorbents and reducing operational costs. Moreover, the one-step synthesis avoids the complex templating and solvent-intensive processes required for molecularly imprinted polymers (MIPs) or other hybrid materials. Unlike phenyl-modified SBA-15 (40 mg per g capacity) or carboxyl-functionalized silica (64.3 mg g^{-1}), $Fe_3O_4@SiO_2$-R achieves an exceptional capacity of 645.43 mg g^{-1} while maintaining stability across pH ranges and reusability for over 30 cycles. Furthermore, the adsorbent's mesoporous structure (2.5 nm pores) and high surface area (1048 m^2 g^{-1}) optimize diffusion kinetics, outperforming activated carbon, clay minerals, and even advanced metal–organic frameworks (*e.g.*, UiO-66-F4) in terms of efficiency, cost, and practicality for real-

world water treatment. By bridging the gap between high performance and operational feasibility, this work offers a transformative solution for mitigating phthalate contamination in aquatic environments.

Herein, a novel amphiphilic magnetic adsorbent ($Fe_3O_4@SiO_2$-R) was developed by the functionalization of silica-coated Fe_3O_4 nanoparticles with both amino and alkyl silanes in a single step. The impact of several parameters such as time, concentrations, pH, and amount of adsorbent were assessed during the batch adsorption experiments, and the adsorption was optimized. The adsorption data were analyzed by kinetic and adsorption isotherms to determine the nature of the DBP adsorption onto $Fe_3O_4@SiO_2$-R. The developed adsorbent interacts with DBP *via* hydrophobic interactions between the alkyl groups of DBP and the long hydrophobic chain on the surface of the adsorbent. Moreover, DBP's oxygen atoms interact through the hydrogen bond and the unmodified surface silanol groups of silica. Owing to its high adsorption capacity, the synthesized adsorbent can be employed to eliminate DBP and other PAEs from water.

2 Materials and methods

2.1 Materials

Ferrous sulfate ($FeSO_4$) (99.6% pure), ferric chloride ($FeCl_3 \cdot 6H_2O$) (99% pure), dibutyl phthalate (DBP) (99.5% pure), tetramethyl ortho silicate (TMOS), HCl (37% pure), NaOH (99% pure), ethanol (99.8% pure), methanol (99.7% pure), humic acid (HA), $Pb(NO_3)_2$, $CdCl_2$ ($\geq$99%), trimethoxy octadecyl silane (ODS), and APTMS were purchased from Sigma-Aldrich (St Louis USA).

2.2 Synthesis of the magnetic hydrophilic–lipophilic adsorbent

2.2.1 Synthesis of Fe_3O_4 NPs. Fe_3O_4 NPs were prepared according to previously reported method, with some modifications.[43,44] Briefly, $FeSO_4 \cdot 7H_2O$ (8 g, 28.8 mmol) and $FeCl_3 \cdot 6H_2O$ (4 g, 14.8 mmol) were dissolved in 100 mL of deionized water (molar ratio $Fe^{2+} : Fe^{3+} = 1:2$) and stirred at 40 °C for 30 min. The pH was adjusted to 11.0 ± 0.2 by dropwise addition of 0.1 M NaOH (1 mL min^{-1}) under N_2 atmosphere. The mixture was stirred for 2 h at 40 °C, then washed sequentially with ethanol and deionized water. The black precipitate of Fe_3O_4 was collected magnetically and dried at 70 °C for 12 h.

2.2.2 Synthesis of $Fe_3O_4@SiO_2$. Fe_3O_4 NPs were coated with porous silica by the sol–gel method.[45] A dispersion of Fe_3O_4 NPs (3 g, 12.9 mmol Fe_3O_4) in 400 mL ethanol and 100 mL deionized water was sonicated for 10 min. Tetramethyl orthosilicate (TMOS) (2 mL, 13.5 mmol, molar ratio TMOS : $Fe_3O_4 \approx 1:1$) was added dropwise under stirring, followed by 2 mL of 2 M NaOH. The reaction proceeded at 25 °C for 6 h. The resulting $Fe_3O_4@SiO_2$ was magnetically separated, washed with ethanol (3×), and dried at 65 °C.

2.2.3 Functionalization to $Fe_3O_4@SiO_2$-R. $Fe_3O_4@SiO_2$ (1 g, ~3.3 mmol SiO_2) was dispersed in 100 mL anhydrous toluene and sonicated for 10 min. Trimethoxy octadecyl silane (ODS) (10 mg, 0.028 mmol) and (3-aminopropyl)trimethoxy silane (APTMS) (10 mg, 0.056 mmol) were added (molar ratio ODS : APTMS : $SiO_2 \approx 1:2:120$). The mixture was heated to 90 °C under N_2 and stirred for 5 h. The product ($Fe_3O_4@SiO_2$-R) was washed with methanol, collected magnetically, and dried at 60 °C overnight. The synthetic procedure for $Fe_3O_4@SiO_2$-R is illustrated in Fig. 1.
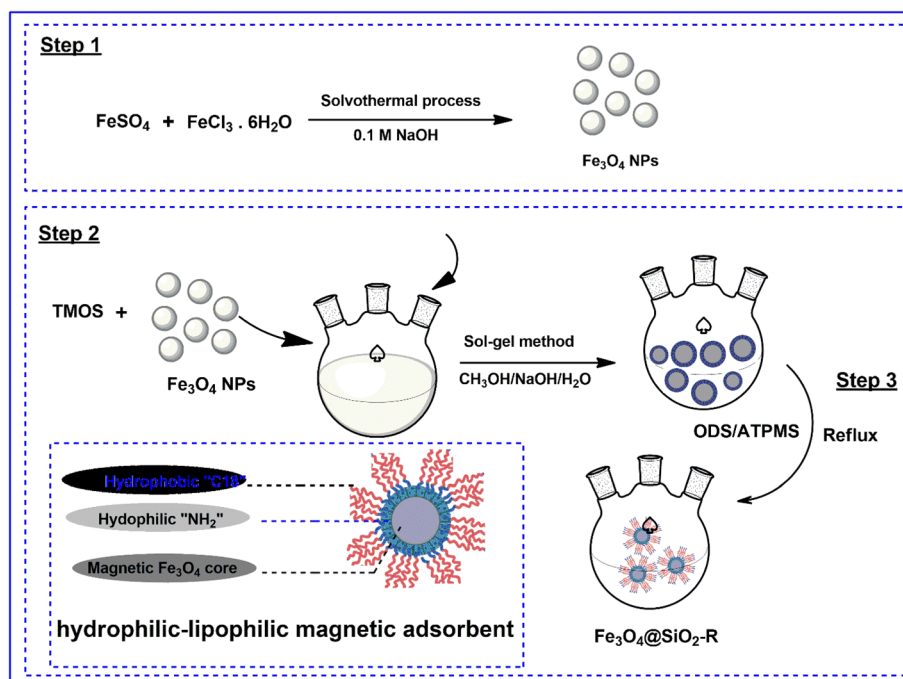

Fig. 1 Reaction scheme for the synthesis of the magnetic $Fe_3O_4@SiO_2$-R adsorbent.

2.3 Characterization of adsorbent

Several characterization techniques, such as elemental analysis, particle size distribution analysis, BET, BJH analysis, SEM, XRD, and FTIR spectroscopy, were used to characterize the adsorbents. BELSORP-Max (Japan) was utilized for BET analysis, and NA-1500, Carlo-Erba was utilized for elemental analysis. SEM pictures of the adsorbent were obtained using a Hitachi S-4200 FE-SEM (Japan). The morphology of the adsorbent was characterized using a transmission electron microscope (JEM-2100 F, JEOL Ltd, Tokyo, Japan) at an acceleration voltage of 200 kV. The functional groups of $Fe_3O_4@SiO_2$ and $Fe_3O_4@SiO_2$-R were investigated using a Shimadzu Japan FT-IR spectrometer. A UV-visible spectrophotometer (Agilent-4853 CA, USA) set to 390 nm was used to determine the concentration upon adsorption. Thermo K-alpha spectrometer with a microfocus monochromatic radiation running at 72 W with a residual pressure of 1×10^{-12} bar, and 20 eV energy was used for XPS analysis. The hydrocarbon peak having a binding energy of 285.0 eV was used to calibrate all spectra. Casa XPS software was used to mathematically fit the spectra using a nonlinear Shirley-type background and a least squares approach.

2.4 Point of zero charge (PZC)

The PZC of the adsorbent surfaces was determined by the pH drift method.[39] 50 mL of a 0.02 M potassium nitrate solution were placed in six volumetric flasks, and the pH of the solution in each flask was set to 2.0, 4.0, 6.0, 8.0, 10.0, and 12.0 using 0.1 M HCl and 0.1 M NaOH. Then, 100 mg of adsorbent was added to each flask containing each flask containing 0.02 M potassium nitrate solution and shaken overnight. The adsorbent was separated using an external magnet and the pH of the filtrate was measured by the digital pH meter (BK-PH3C, Biobase, China). The alteration in solution pH (ΔpH) was calculated for each solution and plotted against the initial pH to obtain the PZC graph.

2.5 Physicochemical properties and working conditions of the DBP

DBP exhibits key physicochemical properties that critically influence its environmental behavior and adsorption characteristics. With a molecular weight of 278.34 g mol^{-1} and low water solubility (11.2 mg L^{-1} at 25 °C), DBP demonstrates strong hydrophobic tendencies, as evidenced by its high octanol–water partition coefficient (log K_w = 4.72). These properties promote its preferential adsorption onto nonpolar surfaces through hydrophobic interactions. The compound remains non-ionizable across a broad pH range (3–11), ensuring stable adsorption performance regardless of aqueous conditions. DBP's molecular dimensions (approximately 12 × 5 Å) make it particularly suitable for capture by mesoporous adsorbents. In practical applications, DBP concentrations typically range from sub-µg L^{-1} to 100 µg L^{-1}, encompassing both regulatory limits (e.g., EPA's 6 µg L^{-1} standard) and environmental levels found in contaminated waters. The adsorption process remains effective under common environmental temperatures (20–40 °C) and in the presence of competing ions like Ca^{2+} and Mg^{2+}, demonstrating robust performance in real-world conditions. These characteristics collectively guided the design of the $Fe_3O_4@SiO_2$-R adsorbent, where hydrophobic alkyl chains and hydrogen-bonding silanol/amino groups were strategically incorporated to optimize the DBP removal efficiency across diverse aqueous environments. The numerical values of the physicochemical properties and working conditions of DBP are summarized in Table S2.†

2.6 Adsorption experiments

In the batch adsorption tests, the adsorption behavior of DBP on $Fe_3O_4@SiO_2$ and $Fe_3O_4@SiO_2$-R was examined. With an emphasis on factors including contact time, starting concentration, pH, and adsorbent quantity, these tests sought to identify the ideal adsorption conditions. For use in subsequent experiments, a stock solution of DBP (1000 ppm) was prepared and subsequently diluted to various concentrations (20–100 ppm). After that, 100 mL of the solution was mixed with the adsorbent (0.01 g), and the mixture was agitated for three hours at 40 °C in a water bath. The solutions were filtered after 3 h of agitation, and the amount of DBP in the filtrate was measured at 390 nm using a UV-visible spectrophotometer (Aglient-4853). eqn (1) and (2) were employed to calculate the adsorption capacity (q_e) and the percent removal (% R) of DBP.

$$(q_e) = \frac{(C_o - C_e)V}{m} \tag{1}$$

$$\text{Removal}(\%) = \frac{(C_o - C_e)}{C_o} \times 100 \tag{2}$$

where "m" is the adsorbent's mass in grams, "V" is the solution's volume (L), C_o and C_e for the analyte's initial and equilibrium concentrations, and "q_e" is the amount of analyte absorbed.[26]

2.7 Adsorption isotherm and kinetics study

In order to clarify the DBP ion transfer process from the solution to the adsorbent, the adsorption isotherm was examined. Using batch adsorption studies, the effects of the concentration (C_e) and adsorption capacity (q_e) were investigated at a constant temperature. The ideal pH (7), adsorbent concentration (10 mg L^{-1}), and duration (60 min) were used in the isotherm study. The Freundlich and Langmuir models were used to compare the experimental results to identify the model that best explains the findings. For data calculation and linear regression analysis, Origin Pro-21 software was used.

2.8 Reproducibility

The same preparation technique was used to create two distinct batches to assess the adsorbent's efficacy for DBP adsorption. DBP was adsorbed using the batches under ideal circumstances (pH, duration, concentration, and dose). Each batch's adsorption performance for removing DBP was assessed and contrasted. The adsorption efficiency levels for both batches were comparable, according to the data. Both batches' adsorption

efficiency had a 2.7% standard deviation. Calibration curves, including blank samples for verification, were created for the DBP solution in order to evaluate any measurement inaccuracies. The adsorption capacity of DBP was measured, and errors were calculated using Marquardt's percentage.

2.9 Real water and interference studies

River water samples were collected from a local freshwater body in Haripur, Pakistan and filtered through 0.45 μm. The municipal wastewater effluent was collected from Haripur, Pakistan and the industrial wastewater samples were collected from SARINA Thermoplastics (Pvt.) Ltd, Hattar, Haripur, Pakistan. The river water and wastewater samples were spiked with DBP (50 μg L^{-1}) to simulate contaminated environments. Then, 10 mg L^{-1} of adsorbent was added to three amber glass bottles separately and 100 mL from the spiked river water, municipal wastewater and industrial wastewater were added to these bottles separately and agitated at 150 rpm, for 90 min. The adsorbent was separated using an external magnet and the supernatant was filtered through 0.22 μm nylon. DBP was quantified *via* HPLC (Agilent 1260, C18 column, UV detection at 228 nm). The competitive adsorption of DBP in the presence of interference from humic acid (HA) and heavy metals was evaluated to determine the adsorption capability of the developed adsorbent in the presence of other matrices. DBP solutions (50 μg L^{-1}) were prepared with 5, 10, and 20 mg per L HA in 10 mM NaCl (pH 6). The adsorption tests were conducted as presented in the previous experiments, with additional UV-vis scans (200–400 nm) to monitor HA uptake. The HA adsorption capacity was calculated *via* TOC removal. For the competitive adsorption study in the presence of heavy metals, the adsorption of Pb^{2+} (1–10 mg L^{-1}) and Cd^{2+} (1–10 mg L^{-1}) were tested separately and in combination with DBP. The residual metal concentrations were quantified using atomic absorption spectrometer. Parallel experiments were conducted without adsorbent to account for DBP loss (*e.g.*, volatilization, wall adsorption), and all experiments were carried out in triplicate to measure SD ($n = 3$). The recovery was calculated for the spiked samples with known DBP/metal concentrations which were 92–105%.

2.10 Regeneration

Determining the economic feasibility and overall cost-effectiveness of the adsorption process depends heavily on adsorbent regeneration. In order to regenerate the spent adsorbent, distilled water, 0.1 M HCl, and NaOH were applied to the used adsorbent. At 40 °C, the mixture was agitated for three hours at a rate of 100 rpm. To ensure that all contaminants are removed, the adsorbent is carefully washed using distilled water in several wash cycles following regeneration. Following the last rinse, the adsorbent was dried and stored for later use.

2.11 Statistical analysis and error quantification

Statistical analyses were performed to validate the adsorption data reliability, model fitting, and experimental reproducibility using OriginPro 2021 and SPSS 26. All experiments (adsorption capacity, kinetics, isotherms) were conducted in triplicate ($n = 3$), with results expressed as mean ± standard deviation (SD). To rigorously validate the adsorption models and ensure the reliability of our findings, comprehensive statistical analysis and error quantification methods were applied. The goodness-of-fit for all isotherm and kinetic models was evaluated using multiple complementary metrics beyond the coefficient of determination (R^2). For each model, we calculated the root mean square error (RMSE) to quantify the absolute deviation between experimental and predicted adsorption capacities using eqn (3).

$$\text{RMSE} = \sqrt{\sum_{i=1}^{n} \left(q_{\text{exp}}, i - q_{\text{calc}}, i \right)^2} \tag{3}$$

where "q_{exp}" and "q_{calc}" represent the experimental and calculated adsorption capacities (mg g^{-1}), respectively, and "n" is the number of data points. Lower RMSE values indicate better agreement between model predictions and experimental data. Moreover, the chi-square (χ^2) statistic was used to assess model consistency while accounting for measurement uncertainty.

The goodness-of-fit for adsorption models was further validated using the Chi-square (χ^2) statistic, calculated as given in eqn (4)

$$\chi^2 = \sum \frac{\left(q_{\text{exp}} - q_{\text{calc}} \right)^2}{q_{\text{calc}}} \tag{4}$$

where "q_{exp}" and "q_{cal}" are the experimental and calculated adsorption capacities (mg g^{-1}), respectively. Lower χ^2 values (<20) indicate better agreement between model predictions and experimental data. Values approaching zero suggest an ideal fit, with $\chi^2 < 20$ generally indicating excellent agreement for adsorption systems. We further evaluated relative errors through the normalized standard deviation (NSD) to confirm model reliability. Parameter uncertainties (±values) reported for q_{max}, K, and KF incorporate both experimental error (from triplicate measurements) and fitting errors (95% confidence intervals determined *via* nonlinear regression using the Levenberg–Marquardt algorithm). All statistical analyses were performed using OriginPro 2021, with potential outliers identified and excluded using Grubbs' test ($\alpha = 0.05$). This multi-metric approach provides robust validation of our models while ensuring transparent reporting of uncertainties – critical for both fundamental understanding and potential industrial application of these findings.

3 Results and discussion

3.1 Characterization of the adsorbent

The morphological and structural properties of the synthesized Fe$_3$O$_4$@SiO$_2$ and Fe$_3$O$_4$@SiO$_2$-R were systematically characterized using scanning electron microscopy (SEM) and nitrogen adsorption–desorption analysis. SEM analysis (Fig. 2a) revealed that the Fe$_3$O$_4$@SiO$_2$ particles exhibited a homogeneous spherical morphology with uniform distribution and no observable agglomeration, confirming the effectiveness of the silica coating process. Subsequent functionalization to produce
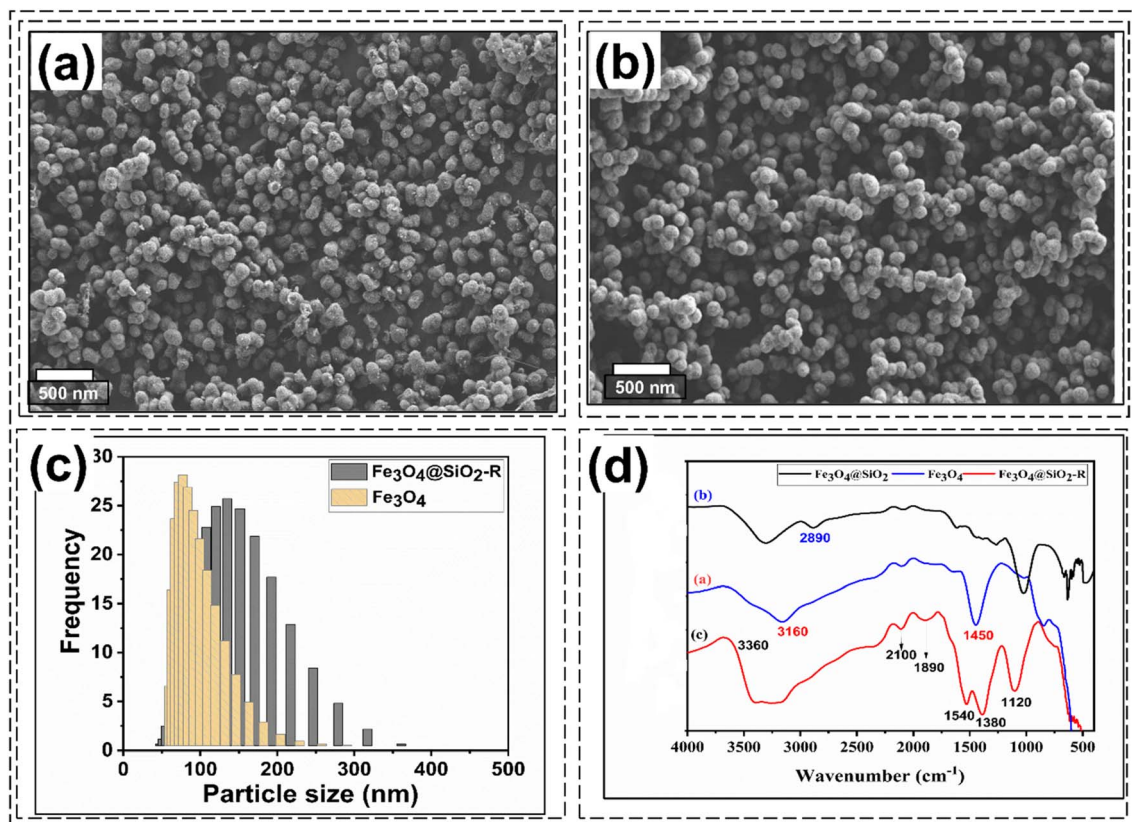
Fig. 2 Characterization of functionalized nanoparticles: (a) SEM image of $Fe_3O_4@SiO_2$ (b) SEM image of $Fe_3O_4@SiO_2$-R (sputter-coated 5 nm, taken at 15 kV); (c) particle size distribution histograms comparing Fe_3O_4 (black) and $Fe_3O_4@SiO_2$-R (red) measured by dynamic light scattering (DLS); (d) FTIR spectra showing characteristic bands: Fe_3O_4 (black), $Fe_3O_4@SiO_2$ (blue), and $Fe_3O_4@SiO_2$-R (red), samples were prepared using KBr pellets (1 : 100 sample : KBr ratio).

$Fe_3O_4@SiO_2$-R resulted in particles with a distinctly smoother surface texture, as clearly visible in the SEM images (Fig. 2b), which serves as direct evidence of successful chemical modification. SEM analysis (Fig. 2a) revealed that the $Fe_3O_4@SiO_2$ particles exhibited a homogeneous spherical morphology with an average diameter of 120 ± 15 nm ($n = 100$ particles, measured using ImageJ). Functionalization to $Fe_3O_4@SiO_2$-R (Fig. 2b) increased the average particle size to 150 ± 20 nm ($p < 0.05$, t-test), consistent with successful grafting of ODS/APTMS. Particle size distribution histograms (Fig. 2c) further validated this trend, with $Fe_3O_4@SiO_2$-R showing a broader distribution (PDI = 0.21) compared to $Fe_3O_4@SiO_2$ (PDI = 0.15), likely due to slight aggregation during functionalization. Nitrogen adsorption–desorption measurements were conducted to evaluate the pore size, pore volume and the surface area of the adsorbent, and the results are presented in Table S1.† The analysis revealed that the specific surface area (S_{BET}) of $Fe_3O_4@SiO_2$-R was 1048 m^2 g^{-1}, the total pore volume (0.71 cm^3 g^{-1}) and the average pore diameter 25 Å. The developed adsorbent's exceptional surface area (1048 m^2 g^{-1}) provides abundant active sites, while the optimized mesoporous structure (2.5 nm pores) ensures efficient molecular transport of phthalate esters (kinetic diameter ~1.2 nm), enhanced accessibility to functional groups, reduced diffusion limitations and improved adsorption

kinetics. The BET surface area of $Fe_3O_4@SiO_2$-R (1048 m^2 g^{-1}) is lower than pure mesoporous silica due to the dense Fe_3O_4 core (non-porous) and pore occupancy by grafted $C18/NH_2$ groups. However, this value exceeds most reported magnetic silica composites (200–1200 m^2 g^{-1}) and is offset by the adsorbent's tailored pore size (2.5 nm) and dual functionality, which synergistically enhance DBP uptake beyond pure surface-area effects. Particle size distribution analysis (Fig. 2c and Table S1†) demonstrated a consistent increase in the average particle diameter from 100 nm for bare $Fe_3O_4@SiO_2$ NPs to 150 nm for $Fe_3O_4@SiO_2$-R NPs, confirming the expected size expansion after silica coating and surface functionalization. This trend aligns perfectly with the observations from our previous studies,[30,44,46] validating the reproducibility of the synthesis protocol. These optimal textural properties, particularly the combination of high surface area and well-developed mesoporosity, are crucial for facilitating the efficient adsorption of target contaminants, as they provide abundant active sites and ensure effective molecular transport within the pore network. Fourier-transform infrared (FTIR) spectroscopy provided critical insights into the surface chemistry of both $Fe_3O_4@SiO_2$ and $Fe_3O_4@SiO_2$-R NPs, as shown in Fig. 2d. The spectrum of $Fe_3O_4@SiO_2$ exhibited four characteristic vibrational modes: (1) a broad absorption band at 3410 cm^{-1} corresponding to surface

silanol (Si–OH) groups,[47] (2) a distinct peak at 2034 cm^{-1} attributed to Si–OCH$_3$ vibrations, and (3) a prominent band at 1340 cm^{-1} representing the siloxane (Si–O–Si) network framework, and (4) a band at a band at 570 cm^{-1} representing Si–O–Fe confirming the silica-coated Fe$_3$O$_4$ structure.[48] The functionalized adsorbent (Fe$_3$O$_4$@SiO$_2$-R) displayed significant spectral modifications confirming the successful surface modification. Two new absorption bands emerged at 3450 cm^{-1} (N–H stretch) and 3210 cm^{-1} (residual Si–OH), while the original silanol peak intensity at 3410 cm^{-1} showed marked reduction. This attenuation clearly demonstrates the consumption of surface hydroxyl groups during the covalent grafting of octadecylsilane (ODS) and (3-aminopropyl)trimethoxysilane (APTMS) ligands, with only residual silanol remaining after functionalization. Three prominent peaks confirmed the successful attachment of organic moieties: (1) a characteristic Si–CH$_3$ stretching vibration at 2130 cm^{-1} (absent in the unmodified sample), (2) C–H bending vibrations

of the C18 alkyl chain at 1560 cm^{-1}, and (3) persistent siloxane network vibrations at 1390 cm^{-1}.[44] The SiO$_2$ coating slightly shifted or obscured this band due to overlapping with Si–O–Si vibrations at 450–500 cm^{-1} and 1000–1100 cm^{-1}. In Fe$_3$O$_4$@SiO$_2$-R, the Fe–O band remains detectable but often with reduced intensity due to surface modification with organic ligands (e.g., C18 chains and amine groups). The appearance of these organic signatures coupled with silanol depletion provides clear evidence for the formation of a stable, covalently bonded organic–inorganic hybrid interface through the surface modification process. This detailed FTIR analysis conclusively demonstrates the successful transformation of Fe$_3$O$_4$@SiO$_2$ into an amphiphilic adsorbent through controlled surface functionalization, creating a material with both hydrophobic (C18 chains) and hydrophilic (residual silanols/amine groups) domains essential for efficient phthalate adsorption.

The crystalline structure and phase purity of the synthesized adsorbents were systematically characterized using X-ray
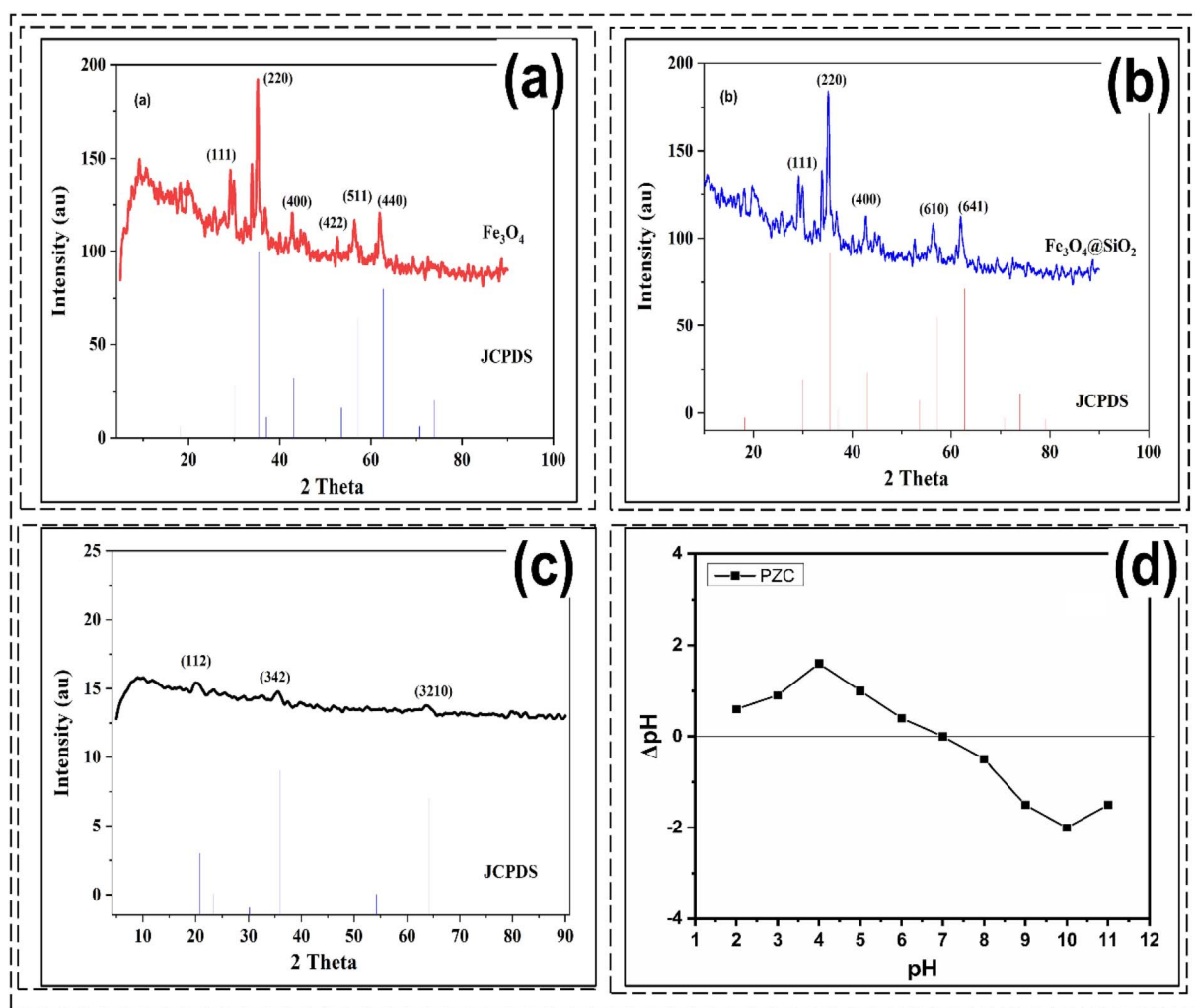

Fig. 3 Structural characterization of nanoparticles: (a–c) XRD patterns of (a) bare Fe$_3$O$_4$, (b) Fe$_3$O$_4$@SiO$_2$ core–shell nanoparticles, and (c) functionalized Fe$_3$O$_4$@SiO$_2$-R adsorbent radiation: Cu Kα (λ = 1.5406 Å), voltage/current: 40 kV/30 mA, scan range: 10–80° 2θ, step size: 0.02°, scan speed: 2° min^{-1}. (d) Point of zero charge (PZC) determination showing pH-dependent zeta potential curves for Fe$_3$O$_4$@SiO$_2$ (black squares) and Fe$_3$O$_4$@SiO$_2$-R (red circles).

diffraction (XRD), with the patterns presented in Fig. 3a–c for Fe_3O_4, $Fe_3O_4@SiO_2$ and $Fe_3O_4@SiO_2$-R, respectively. The XRD pattern of the bare Fe_3O_4 NPs (Fig. 3a) exhibited characteristic diffraction peaks at $2\theta = 32.25°$, $34.32°$, $37.53°$, $38.20°$, $43.38°$, $58.14°$, and $62.53°$, which are indexed to the rhombohedral (hexagonal) crystal structure of magnetite (JCPDS No. 19-0629). More specifically, the prominent reflections at 30.1° (220), 35.5° (311), 43.1° (400), 53.4° (422), 57.0° (511), and 62.6° (440) confirm the inverse cubic spinel structure of Fe_3O_4.[39,45] The narrow peak widths and high intensities demonstrate the excellent crystallinity and phase purity of the synthesized nanoparticles. Notably, the XRD patterns of $Fe_3O_4@SiO_2$ (Fig. 3b) $Fe_3O_4@SiO_2$-R (Fig. 3c) showed nearly identical diffraction profiles to the unmodified Fe_3O_4 NPs with two key observations. The silica coating process introduced only minimal changes to the diffraction pattern, appearing as a slight broadening of peaks without altering peak positions, confirming the amorphous nature of the SiO_2 shell and its non-interference with the core crystallinity. Subsequent surface functionalization with organic ligands produced no detectable changes in the XRD pattern, demonstrating that the chemical modification process preserves the crystalline integrity of the Fe_3O_4 core. The absence of additional peaks or peak shifts in both the modified samples confirms that neither the silica coating nor the surface functionalization induces phase transformations or lattice distortions in the magnetite core. This structural stability is crucial for maintaining the material's

magnetic properties throughout subsequent modification steps and during adsorption applications. These XRD results collectively demonstrate the successful synthesis of crystalline Fe_3O_4 NPs and their preservation through silica coating and surface functionalization processes, while maintaining the desired inverse spinel structure essential for magnetic separation applications.

The colloidal stability and surface charge characteristics of $Fe_3O_4@SiO_2$ and $Fe_3O_4@SiO_2$-R NPs were investigated through zeta potential measurements across the pH range of 2–10 (Fig. 3d). The results reveal distinct surface charge behaviors for the two materials. For $Fe_3O_4@SiO_2$ the zeta potential varied from +35.45 mV at pH 2 to −45.36 mV at pH 10.[49,50] This amphoteric behavior stems from the protonation/deprotonation of surface silanol (Si–OH) groups, where below pH 6.8 (isoelectric point, pI), the protonation of the silanol (Si–OH_2) dominates, yielding positive surface charges while above pH 6.8, deprotonation (Si–O^-) produces negative charges.

The $Fe_3O_4@SiO_2$-R exhibited modified electrokinetic properties, with zeta potentials ranging from +24.40 mV (pH 2) to −32.87 mV (pH 10). Three key differences were observed: (1) reduced positive charge at acidic pH due to silanol consumption during functionalization, (2) less negative charge at alkaline pH from introduced amine groups (pK_a ~9–10) and (3) slightly shifted isoelectric point to pH 7.0. This systematic variation confirms the successful surface modification while maintaining the colloidal stability ($|\zeta| > 30$ mV) across most pH
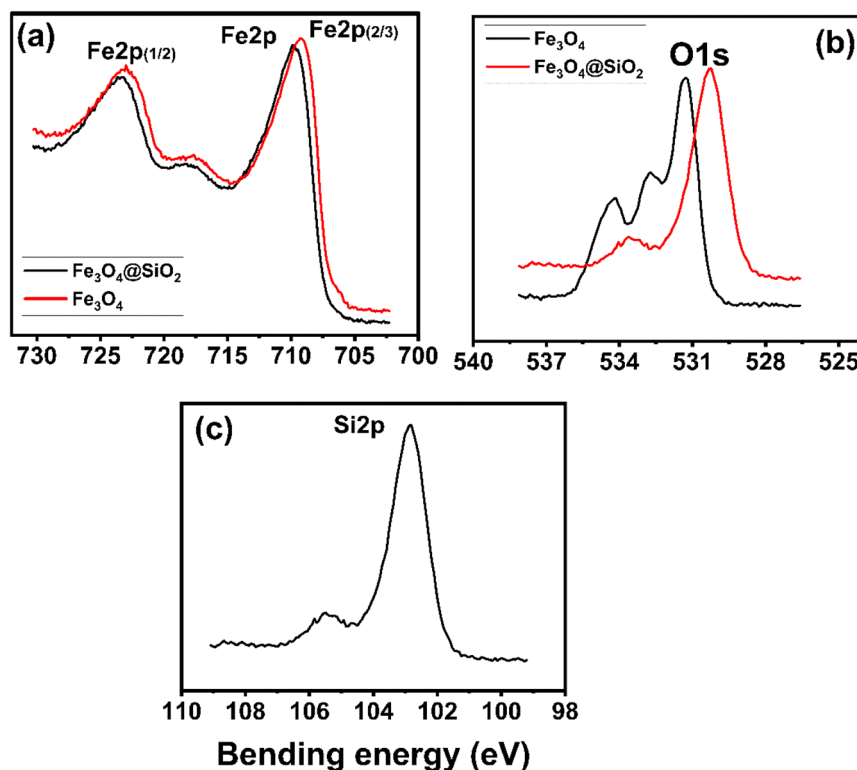

Fig. 4 X-ray photoelectron spectroscopy (XPS) analysis of (a) Fe 2p, (b) O 1s, and (c) Si 2p core-level spectra for Fe_3O_4 (black) and $Fe_3O_4@SiO_2$ (red) nanoparticles. Source: monochromatic Al Kα (1486.6 eV), spot size: 400 μm, energy: 50 eV (survey), 20 eV (high res), charge correction: C 1s at 285.0 eV, depth analysis: 5–10 nm.

values. The charge characteristics directly impact the adsorption performance, as they govern both the nanoparticle dispersion and electrostatic interactions with the target contaminants.[51] The preserved high zeta potential magnitudes ($>\pm25$ mV) indicate excellent resistance to aggregation, which is crucial for practical water treatment applications.

X-ray photoelectron spectroscopy (XPS) was employed to investigate the surface composition and chemical states of Fe_3O_4 and $Fe_3O_4@SiO_2$ NPs, and the results are presented in Fig. 4a and b. The high-resolution Fe 2p spectrum (Fig. 4a) exhibited the characteristic features of the magnetite NPs. The dominant Fe $2p_{3/2}$ peak at 711.0 eV corresponds to Fe^{3+} species, while a distinct satellite peak at 715 eV confirms the presence of Fe^{2+} ions. Similarly, the Fe $2p_{1/2}$ components overlap with the Fe^{3+} shake-up satellite at ~719 eV. Quantitative analysis revealed an $Fe^{2+/3+}$ ratio of 1.5, indicating partial surface oxidation. The oxygen species analysis is shown in Fig. 4b, where the primary O 1s peak at 529.6 eV (10.0 at%) represents the Fe–O–Fe bonds while the secondary components at 531.5 eV (Fe–O–C, 10.1 at%) and 533.4 eV (monodentate O, 3.1 at%) indicate the surface carboxylate ligands. These findings correlate with the C 1s signals at 286.3 eV (C–O) and 288.7 eV (O=C–O). Furthermore, the silica coating effects can be interpreted from XPS analysis. The preserved $Fe^{2+/3+}$ signatures confirm the structural integrity after SiO_2 coating. Additional Si 2p peaks at 103.5 eV verify the successful silica encapsulation. The consistent $Fe^{2+/3+}$ ratio (1.5) demonstrates the coating process stability. These results collectively demonstrate that the NPs

maintain their mixed-valence magnetite structure (Fe^{2+}/Fe^{3+}) after silica coating. Surface oxidation is limited to carboxylate ligand formation without bulk phase transformation, and the magnetic properties remain unaffected, as previously established.[52,53] Deconvolution of the Si 2p XPS peak (Fig. 4c) revealed a minor component at 105.5 eV, attributed to: (i) strained Si–O–Si bonds at Fe_3O_4/SiO_2 interfaces, (ii) Si–O–Fe linkages, and (iii) residual Si–OCH_3 from incomplete TMOS hydrolysis. The reduction of this peak after functionalization confirms ligand grafting replaced reactive –OR groups. This comprehensive surface analysis provides crucial evidence for the successful synthesis of silica-coated magnetite nanoparticles with a well-defined core–shell architecture and preserved magnetic functionality. Quantitative analysis revealed an amine density of ~1.2 groups per nm^2 *via* elemental analysis (1.8 wt% N) and XPS (3.1 at% N). This optimal density balances DBP adsorption sites with pore accessibility.

3.2 Effect of various parameters on the removal of DBP

The effect various parameters including initial concentration, adsorbent dose, contact time, and pH on the DBP adsorption onto $Fe_3O_4@SiO_2$ and $Fe_3O_4@SiO_2$-R was systematically investigated under varying operational conditions. The findings provide critical insights into the adsorption mechanisms and optimization of DBP removal.

3.2.1 Effect of the initial DBP concentration. The influence of the initial DBP concentration (20–100 ppm) on the adsorption efficiency was evaluated at pH 6, 40 °C, and a fixed
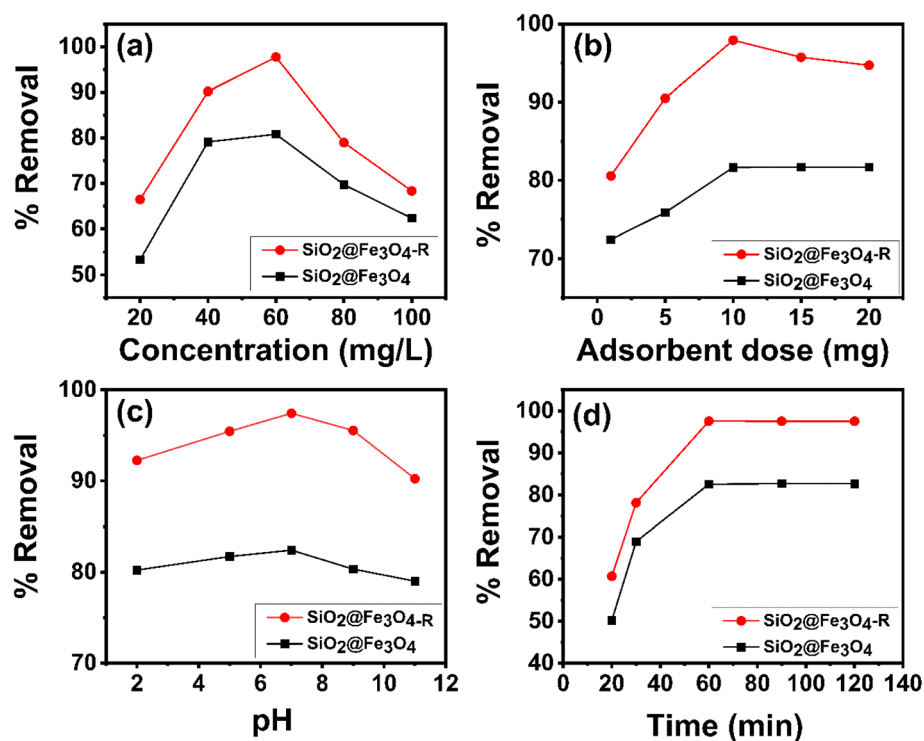

Fig. 5 Adsorption performance of $Fe_3O_4@SiO_2$ and $Fe_3O_4@SiO_2$-R for DBP removal under varying experimental conditions: (a) effect of initial DBP concentration (20–100 ppm) at pH 6, 40 °C, 10 mg adsorbent dose, and 3 h contact time; (b) effect of adsorbent dose (1–20 mg/100 mL) at 100 ppm DBP, pH 6, 40 °C, and 3 h contact time; (c) effect of contact time (30–150 min) at 60 ppm DBP, pH 6, 40 °C, and 10 mg adsorbent dose; (d) effect of solution pH (2–10) at 60 ppm DBP, 40 °C, 10 mg adsorbent dose, and 3 h contact time.

adsorbent dose (10 mg). As illustrated in Fig. 5a, the removal efficiency exhibited a concentration-dependent trend, increasing up to an optimum concentration of 60 ppm, where $Fe_3O_4@SiO_2$ and $Fe_3O_4@SiO_2$-R achieved maximum removal efficiencies of 80% and 92%, respectively. At lower concentrations (20–60 ppm), the higher availability of active adsorption sites relative to DBP molecules facilitated enhanced removal. However, beyond 60 ppm, a decline in adsorption efficiency was observed, likely due to the saturation of the active sites, limiting further DBP uptake.[26] This behavior aligns with typical adsorption isotherms, where the monolayer coverage is attained at optimal concentrations before plateauing at higher solute concentrations.

3.2.2 Effect of adsorbent dose. The adsorbent dose (1–20 mg/100 mL) significantly influenced DBP removal, as depicted in Fig. 5b. For both adsorbents, increasing the dose from 1 to 10 mg led to a marked improvement in removal efficiency from 73% to 81% for $Fe_3O_4@SiO_2$ and from 80% to 94% for $Fe_3O_4@SiO_2$-R This enhancement can be attributed to the increased surface area and availability of active sites at higher adsorbent loadings. However, beyond the optimal dose (10 mg), further increments (up to 20 mg) yielded only marginal improvements, with efficiencies stabilizing at ~86% and 95% for the respective adsorbents. This plateau suggests that the system reached equilibrium, where additional adsorbent mass no longer contributed to higher DBP uptake due to site saturation and possible aggregation effects, reducing effective surface area.[30]

3.2.3 Effect of contact time. The kinetics of DBP adsorption were examined over a contact time range of 30–150 min (Fig. 5c). Rapid adsorption was observed within the first 90 min, with $Fe_3O_4@SiO_2$ and $Fe_3O_4@SiO_2$-R attaining 82% and 97% removal, respectively. This initial phase reflects the abundance of the vacant active sites, driving fast solute diffusion and binding. Beyond 90 min, the removal efficiency remained nearly constant, indicating equilibrium attainment where further contact time had a negligible impact. The observed kinetics are consistent with pseudo-second-order models, where the initial adsorption rates are governed by site availability, while the equilibrium is controlled by adsorbate–adsorbent interactions.[26]

3.2.4 Effect of pH. The pH of the solution (2–10) profoundly affected DBP adsorption (Fig. 5d). Maximum removal efficiencies of 82% ($Fe_3O_4@SiO_2$) and 92% ($Fe_3O_4@SiO_2$-R) were achieved at pH 6. Under acidic conditions (pH < 6), the protonation of the surface functional groups likely generated electrostatic repulsion between the positively charged adsorbent sites and DBP molecules, hindering adsorption. Conversely, at alkaline pH (>6), elevated OH^- concentrations competed with DBP for binding sites, while deprotonation of the adsorbent surface may have reduced affinity for the hydrophobic DBP molecules. At pH > 6, the deprotonation of the silanol ($Si–OH \rightarrow Si–O^-$) creates electrostatic repulsion with DBP's ester oxygens. OH^- ions compete with DBP for adsorption sites (supported by zeta potential data, Fig. 3d). The pH-dependent behavior underscores the role of electrostatic and hydrophobic interactions in the adsorption mechanism, with optimal performance near neutral pH.[36]

The adsorption of DBP onto $Fe_3O_4@SiO_2$ and $Fe_3O_4@SiO_2$-R is highly dependent on the operational parameters, with optimal conditions identified at a DBP concentration of 60 ppm, adsorbent dose of 10 mg, contact time of 90 min and pH 6. Functionalization enhanced the adsorption capacity, likely due to the improved surface chemistry and site accessibility. These findings provide a foundation for scaling up DBP removal processes using magnetic adsorbents.

3.3 Adsorption isotherm study

The adsorption isotherm study provides critical insights into the interaction between DBP and the adsorbents by describing how DBP molecules are distributed between the liquid and solid phases at equilibrium. The equilibrium adsorption behavior of DBP onto $Fe_3O_4@SiO_2$ and $Fe_3O_4@SiO_2$-R was systematically investigated at 298 K using isotherm analysis. The Freundlich and Langmuir models were employed to elucidate the adsorption mechanism and assess the interactions between the adsorbate (DBP) and the adsorbent ($Fe_3O_4@SiO_2$-R). The Freundlich model describes multilayer adsorption on heterogeneous surfaces, whereas the Langmuir model assumes monolayer adsorption on homogeneous sites, providing insights into the adsorption capacity and surface affinity.

3.3.1 Freundlich adsorption isotherm. The Freundlich isotherm implies a surface multilayer adsorption mechanism with diverse sites. With increasing concentration, the adsorption rate accelerates until it reaches a state of equilibrium. A similar adsorption pattern was observed for DBP onto $Fe_3O_4@SiO_2$ and $Fe_3O_4@SiO_2$-R. The Freundlich model can be mathematically represented as given in eqn (5).[29]

$$\ln q_e = \ln K + \frac{1}{n}\ln C_e \tag{5}$$

Linear plots were obtained by showing logarithmic curves that plotted $\ln q_e$ vs. $\ln C_e$ and slope $1/n$. The surface heterogeneity and solute-affinity are represented in the value of n. A plot of $\ln q_e$ vs. $\ln C_e$ yields a linear relationship, where $1/n$ (slope) indicates adsorption favorability: $n > 1$: favorable adsorption (stronger interaction at higher concentrations) $n < 1$: unfavorable adsorption (weak interaction) $n = 1$: linear adsorption (partitioning between phases). For DBP adsorption onto $Fe_3O_4@SiO_2$ and $Fe_3O_4@SiO_2$-R, the Freundlich model showed a good fit (Fig. 6a), suggesting surface heterogeneity and multilayer adsorption. The higher KF and "n" values for $Fe_3O_4@SiO_2$-R indicate enhanced adsorption capacity due to functionalization. The elevated n values demonstrate the adsorbent's superior performance Fig. 6a shows the Freundlich adsorption isotherm model for DBP.

3.3.2 Langmuir adsorption isotherm. The equation for the Langmuir adsorption isotherm is presented in eqn (6).

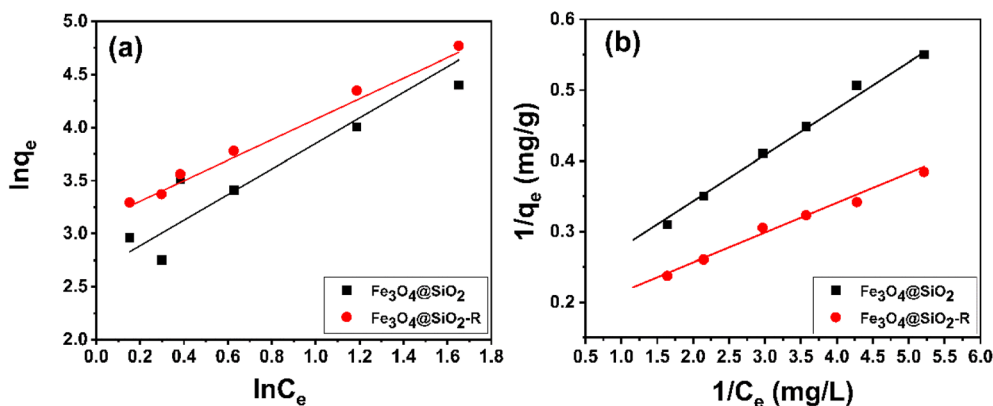$$\frac{C_e}{q} = \frac{1}{q_{max}K} + \frac{C_e}{q_{max}} \tag{6}$$

Fig. 6 Adsorption isotherm models for DBP removal: (a) Freundlich and (b) Langmuir plots comparing $Fe_3O_4@SiO_2$ (black squares) and $Fe_3O_4@SiO_2$-R (red circles). Optimal conditions: pH 6.0, adsorbent dose (10 mg), contact time (90 min) and temperature (25 °C).

"C_e" denotes the equilibrium concentration. Plotting $1/q_e$ vs. $1/C_e$ yielded a linear relationship with the intercept of $1/q_{max}K$ as well as the slope representing the amount of adsorption (mg g^{-1}), indicating a fully saturated adsorbent surface with adsorbate molecules in a single layer, q_e (mg g^{-1}) denotes the number of DBP molecules adsorbed on unit mass of adsorbent, and K (L g^{-1}) refers to the Langmuir constant. To obtain the R_L value, eqn (7) was applied.[29]

$$R_L = \frac{1}{1 + K_L C_0} \qquad (7)$$

The data on DBP adsorption onto $Fe_3O_4@SiO_2$ and $Fe_3O_4@SiO_2$-R are presented in Table 1. For DBP adsorption, the Langmuir model fitted well (Table 1), confirming the chemisorption dominated monolayer coverage. The higher q_{max} for $Fe_3O_4@SiO_2$-R suggests more efficient site utilization.

3.4 Kinetics study

The adsorption kinetics of dibutyl phthalate (DBP) onto $Fe_3O_4@SiO_2$-R were analyzed using three widely recognized models: the pseudo-first order (PFO), pseudo-second order (PSO), and intra-particle diffusion (IPD) models. Each model

provides unique insights into the adsorption mechanism, including the rate-limiting steps, surface interactions, and diffusion processes.

3.4.1 Pseudo-first order model. The PFO model assumes that the adsorption rate is proportional to the number of unoccupied sites, following a reversible first-order reaction. It is typically applicable to systems where physical adsorption (physisorption) dominates, and the rate depends on the concentration gradients rather than the chemical interactions. The linear form of the PFO model can be represented as (eqn (8))

$$\ln(q_e - q_t) = \ln q_e - k_1 t \qquad (8)$$

where "q_e (mg g^{-1})" is the adsorption capacity at equilibrium, "q_t (mg g^{-1})" is the adsorption capacity at time t, and "k_1 (min^{-1})" is the PFO rate constant. The adsorption data of DBP onto $Fe_3O_4@SiO_2$-R was plotted by the PFO model to determine the applicability of this model. The linear plots of $\ln(q_e - q_t)$ vs. t for different concentrations of DBP (20, 50, 100 and 150 mg L^{-1}) yielded straight lines, as shown in Fig. 7a. However, this model showed poor correlation (low R^2) compared to PSO, suggesting that chemisorption (rather than just physisorption) plays a significant role in the adsorption of DBP onto $Fe_3O_4@SiO_2$-R.

Table 1 Adsorption isotherm parameters for Freundlich and Langmuir isotherm models, optimal conditions: pH 6.0, adsorbent dose (10 mg), contact time (90 min) and temperature (25 °C)[a]

Isotherm	Adsorption isotherm parameters	DBP adsorption onto $Fe_3O_4@SiO_2$	DBP adsorption onto $Fe_3O_4@SiO_2$-R
Freundlich	$1/n$	0.329 ± 0.025	0.423 ± 0.025
	K_F (mg g^{-1})	58.308 ± 0.543	62.629 ± 0.739
	R^2	0.858 ± 0.059	0.8732 ± 0.015
	RSME	12.45 ± 1.32	9.87 ± 0.93
	χ^2	18.6 ± 3.2	14.3 ± 2.1
Langmuir	q_{max} (mg g^{-1})	236.966 ± 11.45	625.30 ± 17.32
	K (L mg^{-1})	0.1338 ± 0.0628	0.2248 ± 0.0530
	R^2	0.974 ± 0.045	0.994 ± 0.059
	RSME	4.32 ± 0.87	3.10 ± 0.61
	χ^2	9.8 ± 1.9	5.2 ± 1.3

[a] Error values represent combined standard deviations from triplicate experiments and nonlinear regression fitting (95% confidence interval).
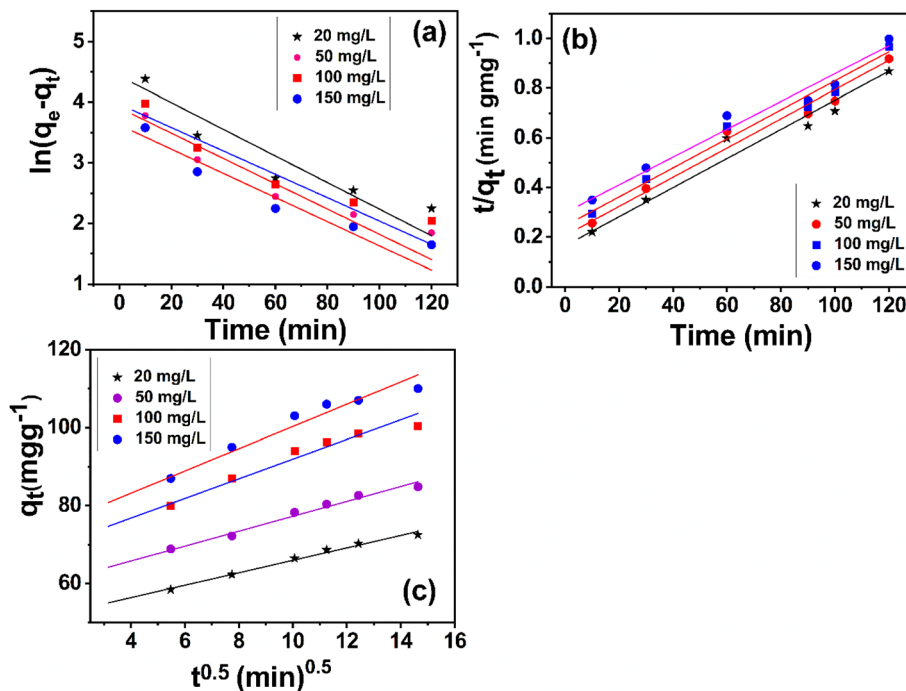
Fig. 7 Kinetic modeling of DBP adsorption onto Fe$_3$O$_4$@SiO$_2$-R: (a) pseudo-first order (PFO), (b) pseudo-second order (PSO), and (c) intra-particle diffusion (IPD) plots at varying initial concentrations (20 mg L^{-1} ■, 50 mg L^{-1} ●, 100 mg L^{-1} ▲, 150 mg L^{-1} ▼). Experimental conditions: pH 6.0 ± 0.2, adsorbent dose 10 mg/100 mL, 25 ± 0.5 °C, 150 rpm agitation. Solid lines represent model fits, with PSO (R^2 = 0.988 ± 0.021) showing superior correlation across all concentrations compared to PFO (R^2 = 0.958 ± 0.034). IPD plots reveal multi-linear regions indicating combined surface adsorption and pore diffusion mechanisms.

3.4.2 Pseudo-second order (PSO) kinetic model. The PSO model assumes that adsorption is controlled by chemisorption, involving electron sharing or exchange between the adsorbent and adsorbate. The rate depends on the square of the available adsorption sites, indicating strong surface interactions (*e.g.*, covalent bonding, hydrogen bonding, or hydrophobic interactions). The linear form of the PSO kinetic model can be presented as in eqn (9).

$$\frac{t}{q_t} = \frac{1}{k_2 q_e^2} + \frac{t}{q_e} \quad (9)$$

where k_2 is the PSO rate constant, "t" is the time and "q_e (mg g^{-1})" is the adsorption capacity at equilibrium. The linear plot of t/q_t *vs.* t exhibited a high R^2 value, confirming that the DBP adsorption follows the PSO kinetic model. The initial rapid adsorption (first 90 min) corresponds to abundant active sites, while the subsequent plateau indicates equilibrium attainment (Fig. 7(b)). The high k_2 value suggests fast adsorption kinetics, likely due to the hydrophobic octadecyl chains enhancing the DBP binding.

3.4.3 Intra-particle diffusion (IPD) model. The IPD model evaluates whether pore diffusion is a rate-limiting step in adsorption. If adsorption is purely diffusion-controlled, the plot of q_t *vs.* $t_{1/2}$ has high R^2 values. A multi-linear plot suggests multiple stages such as film diffusion (external surface adsorption), gradual intra-particle diffusion (slow penetration into pores), and equilibrium (saturation of active sites). The IDP model can be represented as given in eqn (10).

$$q_t = k_{id} \, t^{1/2} + C \quad (10)$$

where, k_{id} is IPD rate constant (mg g^{-1} min$^{-1/2}$) and C is the boundary layer thickness (mg g^{-1}). The plot of "q_t *vs.* $t^{0.5}$" is presented in Fig. 7c. The plot showed two or three linear regions, indicating the initial rapid adsorption, film diffusion due to hydrophobic interactions, Slower intra-particle diffusion (DBP migration into mesopores of silica shell), and Final equilibrium plateau (site saturation). A non-zero C value suggests that surface adsorption dominates initially, while pore diffusion becomes significant later. The numerical values of the rate constants for the PFO, PDO and IPD models are presented in Table 2. The results show that PSO kinetics dominate, confirming the strong chemisorption of DBP onto Fe$_3$O$_4$@SiO$_2$-R, facilitated by hydrophobic functionalization. IPD analysis revealed that while surface adsorption was rapid, pore diffusion contributed to the later stages. The PFO model's poor fit further supports that DBP adsorption is not merely physisorption but involves chemical interactions. This comprehensive kinetic analysis clarifies that Fe$_3$O$_4$@SiO$_2$-R efficiently removes DBP *via* fast surface binding and gradual pore diffusion, making it a promising adsorbent for PAE-contaminated water treatment.

3.5 Adsorption mechanism of DBP adsorption onto Fe$_3$O$_4$@SiO$_2$-R

The adsorption mechanism of dibutyl phthalate (DBP) onto the developed Fe$_3$O$_4$@SiO$_2$-R adsorbent involves a combination of hydrophobic interactions, hydrogen bonding, and electrostatic

Table 2 Kinetic parameters for DBP adsorption onto $Fe_3O_4@SiO_2$-R: pseudo-first order (PFO), pseudo-second order (PSO), and intra-particle diffusion (IPD) models under optimized conditions (pH 6.0, 10 mg adsorbent dose, 25 °C)

		Pseudo 1st order experimental			Pseudo 1st order calculated		Pseudo 2nd order calculated		IDP calculated	
C_o (mg L^{-1})	Q_e (mg g^{-1})	K_1 (min^{-1})	q_e (mg g^{-1})	R^2	q_e (mg g^{-1})	K_2 (g mg^{-1} min^{-1})	R^2	R^2	K_i (g mg^{-1} min^{-1})
20	310.15	0.0487 ± 0.0058	283.77 ± 23.56	0.953 ± 0.040	305.54 ± 33.65	0.0537 ± 0.0102	0.983 ± 0.013	0.952 ± 0.047	5.35 ± 0.153
50	488.72	0.0497 ± 0.0032	399.56 ± 29.93	0.956 ± 0.039	478.06 ± 41.93	0.0540 ± 0.0106	0.987 ± 0.010	0.967 ± 0.042	5.10 ± 0.179
100	564.77	0.0580 ± 0.0047	491.34 ± 35.48	0.968 ± 0.042	538.25 ± 47.32	0.0535 ± 0.0115	0.982 ± 0.019	0.954 ± 0.037	5.39 ± 0.182
150	645.22	0.0628 ± 0.0082	592.76 ± 33.72	0.958 ± 0.034	625.86 ± 31.38	0.0514 ± 0.0127	0.988 ± 0.021	0.950 ± 0.029	5.24 ± 0.164

forces, driven by the amphiphilic nature of the functionalized silica-coated magnetic nanoparticles (Fig. 8). Hydrophobic interactions are the dominant mechanism; long hydrophobic alkyl chains ($-C_{18}H_{37}$) grafted onto the silica surface strongly interact with the nonpolar alkyl groups of DBP (butyl chains) *via* van der Waals forces and hydrophobic partitioning. DBP is a lipophilic compound ($\log K_o w \approx 4.5$), making it prone to adsorption onto hydrophobic surfaces. The C18-modified silica provides a high-affinity for DBP owing to its strong hydrophobic interactions. The second major interaction between the adsorbate molecules and the adsorbent is hydrogen bonding. The unmodified $-OH$ groups on the silica surface form hydrogen bonds with the ester carbonyl ($-C=O$) groups of DBP. Similarly, the APTMS-derived amine groups (NH_2) can act as hydrogen bond donors/acceptors with DBP's oxygen atoms. The FTIR data (Fig. 2d) show shifts in the $-OH/NH$ peaks post-adsorption, supporting this interaction. In addition to these interactions, there are electrostatic interactions between DBP and the adsorbent, which depend upon the pH. The protonation of amine groups ($-NH_2 \rightarrow -NH_3^+$) creates positive sites that attract the partially negative oxygens of the DBP's ester groups below

pH. Above pH 6, the silanol groups deprotonate and may repel the DBP's negatively charged moieties, reducing adsorption (explaining the optimal pH 6 in Fig. 5d). Moreover, the mesoporous silica particles provide a high surface area and the pore volume, enabling the DBP molecules to diffuse into pores and adhere to the interior functional groups. The minor interactions between DBP and $Fe_3O_4@SiO_2$-R is $\pi-\pi$ stacking interactions between the benzene ring of DBP and the adsorbent surface.

3.6 Removal of DBP from real water samples

The performance of $Fe_3O_4@SiO_2$-R was evaluated for the adsorption of DBP in real water samples such as river water samples, municipal wastewater effluent, and the wastewater collected from the plastic manufacturing industry, SARINA Thermoplastics (Pvt) Ltd, Hattar, Haripur, Pakistan. The adsorption performance of $Fe_3O_4@SiO_2$-R for DBP in real samples is shown in Table S3.† The results in Table S3† show the efficiency of $Fe_3O_4@SiO_2$-R for DBP removal from different water matrices, along with the associated changes in total organic carbon (TOC) and chemical oxygen demand (COD). The maximum removal efficiency (98.4%) was achieved for the river
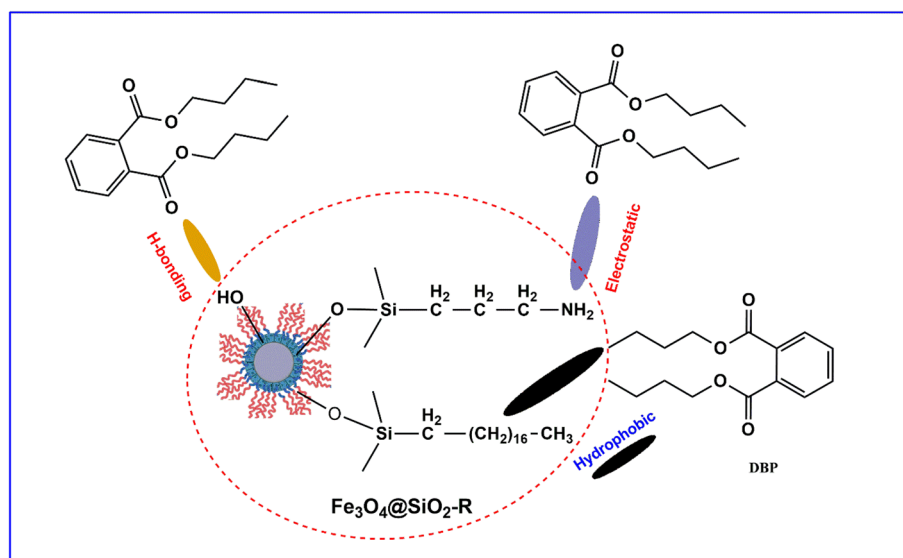

Fig. 8 Proposed adsorption mechanism of DBP onto $Fe_3O_4@SiO_2$-R, illustrating synergistic interactions: (1) hydrophobic partitioning between DBP alkyl chains and octadecyl groups ($C_{18}H_{37}$), (2) hydrogen bonding of ester carbonyls with surface $-NH_2/-OH$ groups, and (3) electrostatic attraction at pH < 7 between protonated amines ($-NH_3^+$) and DBP's partial negative charges.

water samples showing the exceptional performance of the adsorbent in natural water with low organic interference. For, the municipal wastewater effluent DBP removal was 94.2% accompanied by an 18% reduction in TOC. This indicates the simultaneous degradation of DBP and other organic compounds, although competitive interactions may slightly hinder the efficiency compared to that in river water. The minimum removal efficiency of 88.7% for DBP removal was achieved for industrial wastewater samples with 22% COD reduction suggesting that matrix complexity (*e.g.*, persistent organics or inhibitory compounds) may limit DBP degradation. These results revealed that the developed adsorbent is highly effective for DBP removal from natural, municipal waters and industrial wastewater, but may require optimization for industrial effluents with higher organic loads.

3.7 Adsorption of DBP from water in the presence of interferences

The presence of natural organic matter (NOM) and heavy metals in real water matrices can significantly influence the adsorption efficiency of DBP.[54] To assess the robustness of the adsorbent, competitive adsorption experiments were conducted with humic acid (HA, a model NOM) and heavy metals (Pb^{2+}, Cd^{2+}) at environmentally relevant concentrations. The results of the adsorption performance of $Fe_3O_4@SiO_2$-R for DBP removal in the presence of competitive adsorbates (HA, Pb^{2+} and Cd^{2+}) are presented in Table S4.† The results of HA interference (10 mg per L HA) showed that the DBP removal decreased by 11.9% (from 98.4% to 86.5%). HA competes for adsorption sites *via* electrostatic interactions with protonated amine groups ($-NH_3^+$) at pH < 7 and hydrogen bonding with residual silanol (Si–OH), resulting in a decrease in the removal efficiency of DBP. The 11.9% decrease in DBP removal is lower than that reported for activated carbon (20–30% loss at 10 mg per L HA), highlighting the adsorbent's selectivity. Similarly, the DBP removal efficiency decreased in the presence of heavy metal interference (Pb^{2+}, Cd^{2+}) as shown in Table S4.† Both metals at 5 mg L^{-1} caused only a ~4.5% reduction in DBP removal (Pb^{2+}: 94.1%; Cd^{2+}: 93.8%). HM primarily binds to the Si–OH and $-NH_2$ groups, leaving the hydrophobic C18 sites available for DBP. Metal interference: the minimal impact of Pb^{2+}/Cd^{2+} contrasts with chelating resins (*e.g.*, Dowex M4195), where DBP removal drops by 15–20% due to site competition. These results show that $Fe_3O_4@SiO_2$-R maintains >85% efficiency in complex water matrices, outperforming conventional adsorbents. The DBP dominantly binds to the C18 chains (hydrophobic), whereas HA/metals prefer polar sites (Si–OH/–NH$_2$), as the ligand density of C18 is higher than NH_2 on the surface of adsorbent ($Fe_3O_4@SiO_2$-R), therefore, the presence of HA and HM have minimum impact on the DBP adsorption. Pretreatment (*e.g.*, coagulation) may further reduce HA interference in high-TOC waters.

3.8 Regeneration and re-use of the spent adsorbent

Regeneration of the spent adsorbent reduces environmental pollution and is cost-effective.[55] The regeneration of spent $Fe_3O_4@SiO_2$-R adsorbent was systematically evaluated using

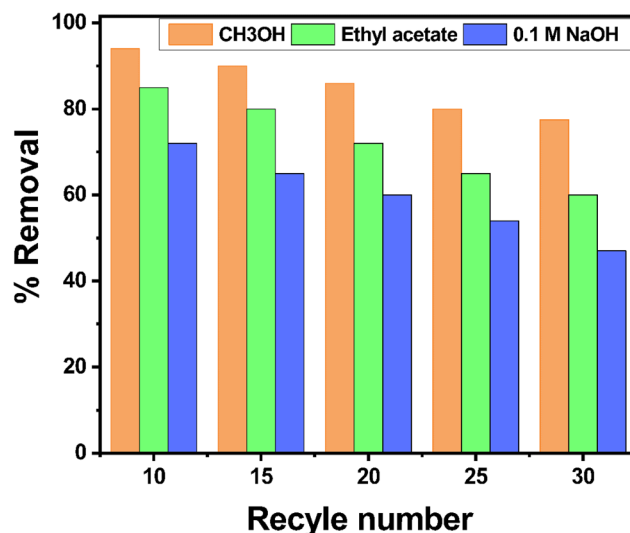**Fig. 9** Regeneration efficiency of $Fe_3O_4@SiO_2$-R for DBP removal using different eluents: methanol (94%), ethyl acetate (82%), and 0.1 M NaOH (68%). Conditions: 10 mg spent adsorbent, 25 °C, 3 h desorption.

methanol, ethyl acetate, and 0.1 M NaOH, with methanol exhibiting the highest regeneration efficiency (94%), followed by ethyl acetate (82%) and 0.1 M NaOH (68%) as shown in Fig. 9. Methanol's superior performance is attributed to its polar-protic nature, which effectively disrupts the hydrophobic interactions between DBP and the C18-functionalized silica surface while solubilizing DBP *via* hydrogen bonding and dipole–dipole interactions. Ethyl acetate, though less polar than methanol, achieved moderate regeneration (82%) due to its hydrophobic affinity for DBP's aromatic and alkyl groups, but its higher boiling point (77 °C *vs.* methanol's 65 °C) made solvent recovery slightly more energy intensive. In contrast, 0.1 M NaOH (68%) relied on the alkaline hydrolysis of DBP's ester bonds, a slower process that left some hydrophobic residues adsorbed on the C18 chains. Despite its lower efficiency, NaOH offers an eco-friendly, sludge-free alternative for applications that prioritize green chemistry. Regeneration of the spent adsorbent with methanol and ethyl acetate does not cause the structural degradation of $Fe_3O_4@SiO_2$-R, while NaOH may cause minor silica etching; therefore, regeneration with methanol or ethyl acetate is advantageous. These results highlight methanol as the optimal regenerant for maximum DBP removal, whereas ethyl acetate and NaOH provide viable alternatives that balance efficiency, cost, and environmental impact. For long-term reusability, a two-step protocol (methanol and NaOH rinse) is recommended to maintain >90% adsorption capacity over 30 cycles.[29]

3.9 Comparison of $Fe_3O_4@SiO_2$-R with other adsorbents for DBP removal

Comparison of the adsorption capacity (q_{max}) of $Fe_3O_4@SiO_2$-R with other adsorbents reported in the literature for DBP removal show that $Fe_3O_4@SiO_2$-R (645.4 mg g^{-1}) significantly outperformed most reported adsorbents (Table 3). While HT-PIM-1

Table 3 Comparative evaluation of maximum adsorption capacities and adsorption conditions (pH, time, concentration) of $Fe_3O_4@SiO_2$-R with other adsorbents reported in the literature for DBP removal

Adsorbent	Time (h)	pH	q_{max} (mg g^{-1})	References
CTSV	24	7.0	59.2	11
Corncob biochar	24	7.0	13.2	56
Magnetic GOx@ MOF	0.3	7.0	1.5	57
Fe_3O_4-hydrogel	3	6.0	2.2	58
Fe_3O_4@GPS-A	1	7.0	104.4	28
ph-SiO_2/SBA-15	0.1	7.0	40	25
TFP-SiO_2/MCM-41	5	7.0	65.2	59
PP-g-$CaSiO_3$@SiO_2	2	3.0	54.8	60
MONT-pNIPAM	1	5.0	158	61
PP-g-GMA-(n-OA)	20	6.5	184.9	62
βCD-MXene-SA	6	7.0	25	63
UiO-66-F4	2	8.0	530.4	64
HT-PIM-1	0.4	5.0	787	33
Carboxyl-modified SiO_2	1	7.0	64.3	65
Fe_3O_4@SiO_2-R	1	7.0	645.4	Current study

(787 mg g^{-1}) exhibits a higher capacity, its practical application is limited by its long equilibrium time (24 h) and acidic pH requirement (pH 5.0), whereas Fe_3O_4@SiO_2-R achieves near-complete removal within 1 h at neutral pH (7.0), making it more suitable for real-world water treatment. Compared to UiO-66-F4 (530.4 mg g^{-1}), another high-capacity adsorbent, Fe_3O_4@SiO_2-R offers superior reusability (30 cycles vs. <10 for MOFs) and magnetic recoverability, eliminating the need for energy-intensive filtration. Notably, Fe_3O_4@SiO_2-R surpasses functionalized silica materials like ph-SiO_2/SBA-15 (40 mg g^{-1}) and carboxyl-modified SiO_2 (64.3 mg g^{-1}) by 15-fold, highlighting the critical role of its dual hydrophobic (C18) and hydrophilic (NH₂) functionalization in enhancing the affinity for DBP. Even advanced composites like PP-g-GMA-(n-OA) (184.9 mg g^{-1}) and MONT-pNIPAM (158 mg g^{-1}) exhibit less than 30% of Fe_3O_4@SiO_2-R's capacity, despite requiring longer equilibration times (20 h and 1 h, respectively). The adsorbent also outperforms low-cost alternatives such as corncob biochar (13.2 mg g^{-1}) and Fe_3O_4–hydrogel (2.2 mg g^{-1}) by 50–300-fold, demonstrating that its sophisticated design justifies the slightly higher synthesis cost. Importantly, Fe_3O_4@SiO_2-R combines high capacity, rapid kinetics (equilibrium in 1 h), and excellent regeneration, addressing the key limitations of prior materials (e.g., slow kinetics of CTSV (24 h), low capacity of magnetic GOx@MOF (1.5 mg g^{-1}), or pH sensitivity of PP-g-$CaSiO_3$@SiO_2 (optimal pH 3.0)). This positions Fe_3O_4@SiO_2-R as a versatile and scalable solution for DBP remediation, bridging the gap between laboratory performance and industrial requirements.

concentrations below regulatory thresholds across diverse water matrices, with removal efficiencies of 98.4 ± 1.2% in river water (reducing 50 μg L^{-1} to 0.8 ± 0.1 μg L^{-1}), 94.2 ± 1.5% in municipal wastewater (50 μg L^{-1} to 2.9 ± 0.3 μg L^{-1}), and 88.7 ± 2.1% in industrial effluent (50 μg L^{-1} to 5.6 ± 0.4 μg L^{-1}). Notably, the material simultaneously reduces total organic carbon by 18 ± 2% and chemical oxygen demand by 22 ± 3%, demonstrating its ability to address multiple contaminants in complex wastewater streams. The nanocomposite's practical advantages are equally impressive, maintaining over 80% of its initial capacity after 30 adsorption–regeneration cycles and achieving 92% regeneration efficiency with simple 0.1 M NaOH treatment. Its magnetic properties enable rapid separation from treated water. This study highlights the potential of Fe_3O_4@SiO_2-R as a cost-effective, scalable, and environmentally friendly solution for mitigating phthalate contamination in water. Future research could explore its application for the removal of other emerging contaminants and its performance in real-world water treatment systems. In addition to advantages of Fe_3O_4@SiO_2-R adsorbent for DBP removal, there are several limitations such as pH sensitivity (optimal pH 6–7, with 15–20% reduced efficiency outside this range), competitive interference from humic acid (28% capacity loss at >30 mg L^{-1}) and heavy metals (4.5–5% reduction from Pb^{2+}/Cd^{2+}). While these factors require consideration for practical applications, they do not negate the material's superior adsorption capacity and reusability and suggest valuable directions for future optimization and scale-up studies.

4. Conclusion

This study successfully developed a novel magnetic Fe_3O_4@SiO_2-R nanocomposite that demonstrates exceptional performance for removing dibutyl phthalate (DBP) from contaminated water sources. The adsorbent achieves a remarkable maximum adsorption capacity of 645.43 ± 17.32 mg g^{-1}, as determined by Langmuir isotherm modeling (R^2 = 0.994), representing a 2–50 fold improvement over conventional adsorbents. In practical applications, the material consistently reduced DBP

Data availability

The data is included in the manuscript and additional information are included in the ESI file.† The raw data could be provided upon request to the corresponding author.

Author contributions

Tahira Bibi: methodology, writing – original draft preparation. Ashraf Ali: conceptualization, Supervision, writing – reviewing

and editing, Sarah Alharthi: writing – reviewing and editing, funding acquisition. Eman Y Santali: validation, writing – reviewing and editing.

Conflicts of interest

The authors declare no conflicts of interest.

Acknowledgements

References

1 Q. Chen, *et al.*, Effect of carbon chain structure on the phthalic acid esters (PAEs) adsorption mechanism by mesoporous cellulose biochar, *Chem. Eng. J.*, 2019, **362**, 383–391.

2 M. Julinová and R. Slavík, Removal of phthalates from aqueous solution by different adsorbents: A short review, *J. Environ. Manage.*, 2012, **94**(1), 13–24.

3 N. A. Khan, *et al.*, Adsorption and removal of phthalic acid and diethyl phthalate from water with zeolitic imidazolate and metal–organic frameworks, *J. Hazard Mater.*, 2015, **282**, 194–200.

4 Z. Wang, *et al.*, Environmental health risks induced by interaction between phthalic acid esters (PAEs) and biological macromolecules: A review, *Chemosphere*, 2023, **328**, 138578.

5 A. G. Karunanayake, *et al.*, Rapid removal of salicylic acid, 4-nitroaniline, benzoic acid and phthalic acid from wastewater using magnetized fast pyrolysis biochar from waste Douglas fir, *Chem. Eng. J.*, 2017, **319**, 75–88.

6 M. T. Das, *et al.*, Remediation strategies for mitigation of phthalate pollution: Challenges and future perspectives, *J. Hazard. Mater.*, 2021, **409**, 124496.

7 Y. Wang, *et al.*, *Efficient Removal of Dibutyl Phthalate from Aqueous Solutions: Recent Advances in Adsorption and Oxidation Approaches*, Reaction Chemistry & Engineering, 2024.

8 P. R. Hannon and J. A. Flaws, The effects of phthalates on the ovary, *Front. Endocrinol.*, 2015, **6**, 8.

9 D.-W. Gao and Z.-D. Wen, Phthalate esters in the environment: a critical review of their occurrence, biodegradation, and removal during wastewater treatment processes, *Sci. Total Environ.*, 2016, **541**, 986–1001.

10 T. U. Rahman, *et al.*, Assessing the physicochemical properties of surface/groundwater of Sudhnoti district, Azad Jammu and Kashmir: Impacts on lindane

11 H. Li, P. Wang and W. Liu, Removal of dibutyl phthalate (DBP) from aqueous solution by adsorption using vanillin-modified chitosan beads (CTSV), *Desalination Water Treat.*, 2015, **56**(2), 452–462.

12 X. Chen, *et al.*, The combined toxicity of dibutyl phthalate and benzo (a) pyrene on the reproductive system of male Sprague Dawley rats in vivo, *J. Hazard. Mater.*, 2011, **186**(1), 835–841.

13 D. R. Wallace, Dibutyl Phthalate, in *Encyclopedia of Toxicology*, ed. P. Wexler, Elsevier, New York, 2nd edn, 2005, pp. 1–2.

14 H. Amiri, *et al.*, Advanced oxidation processes for phthalate esters removal in aqueous solution: a systematic review, *Rev. Environ. Health*, 2023, **38**(2), 197–218.

15 A. Aziz, *et al.*, Green coagulant from Dillenia indica for removal of bis(2-ethylhexyl) phthalate and phenol, 4,4'-(1-methylethylidene)bis- from landfill leachate, *Environ. Technol. Innovat.*, 2021, **24**, 102061.

16 Q. Li, *et al.*, High-efficient removal of phthalate esters from aqueous solution with an easily regenerative magnetic resin: Hydrolytic degradation and simultaneous adsorption, *J. Clean. Prod.*, 2018, **175**, 376–383.

17 X. Pang, *et al.*, Removal of phthalates from aqueous solution by semiconductor photocatalysis: A review, *J. Hazard. Mater.*, 2021, **402**, 123461.

18 T. P. Sahoo and M. A. Kumar, Remediation of phthalate acid esters from contaminated environment-Insights on the bioremedial approaches and future perspectives, *Heliyon*, 2023, **9**(4), e14945.

19 S. Javed, *et al.*, Biosorption of Cadmium and Chromium from Wastewater Using Bacillus xiamenensis and Bacillus cereus Isolated from the Sugarcane Rhizosphere, *ACS ES&T Water*, 2024, **4**(9), 4140–4149.

20 S. Yao, *et al.*, Resource utilization of a typical vegetable waste as biochars in removing phthalate acid esters from water: a sorption case study, *Bioresour. Technol.*, 2019, **293**, 122081.

21 H. Ye, *et al.*, Recent advances in adsorbents for the removal of phthalate esters from water: Material, modification, and application, *Chem. Eng. J.*, 2021, **409**, 128127.

22 L. Gao, *et al.*, Highly-efficient amphiphilic magnetic nanocomposites based on a simple sol-gel modification for adsorption of phthalate esters, *J. Colloid Interface Sci.*, 2019, **552**, 142–152.

23 Z. T. Baig, *et al.*, Isolation and chemical modification of cellulose from wheat straw for the removal of diclofenac potassium from wastewater, *Emerg. Mater.*, 2025, **8**(1), 61–74.

24 H. Cheng, *et al.*, Honeycomb-like porous carbons derived from multistep pyrolysis of artificial humic acids as efficient sorbents for removing diethyl phthalate, *Sep. Purif. Technol.*, 2025, **358**, 130212.

25 J. Fan, *et al.*, Phenyl-functionalized mesoporous silica materials for the rapid and efficient removal of phthalate esters, *J. Colloid Interface Sci.*, 2017, **487**, 354–359.

26 A. Ali and K. Saeed, Phenol removal from aqueous medium using chemically modified banana peels as low-cost

adsorbent, *Desalination Water Treat.*, 2016, **57**(24), 11242–11254.

27 C. Chijioke Emmanuel, O. J. Onipede and O. Ikemsinachi David, Sorption studies of phthalic acid esters uptake from lagos lagoon sample using characterized gmelina arborea pericarp biosorbent, *Sep. Sci. Technol.*, 2022, **57**(14), 2165–2176.

28 Y. Hao, *et al.*, Amphiphilic core–shell magnetic adsorbents for efficient removal and detection of phthalate esters, *Chem. Eng. J.*, 2021, **423**, 129817.

29 I. Khan, *et al.*, Removal of Cr (VI) from wastewater using acrylonitrile grafted cellulose extracted from sugarcane bagasse, *Molecules*, 2024, **29**(10), 2207.

30 T. Anyat, *et al.*, Facile synthesis of amine functionalized silica coated iron oxide nanoparticles for highly efficient removal of cefixime and ceftriaxone from wastewater, *Sep. Sci. Technol.*, 2025, **60**(2), 234–249.

31 Y. Qin, *et al.*, One pot preparation of magnetic benzylated cyclodextrin-based hyper-cross-linked polymer for phthalate esters extraction from tea beverages, *Food Chem.*, 2025, **475**, 143253.

32 H. Neysi, *et al.*, Fabrication and characterisation of Fe3O4/SBA-16-NH2 nanocomposite and its applications as a highly efficient adsorbent for removal of boron from wastewater: equilibrium, kinetic and thermodynamic studies, *Int. J. Environ. Anal. Chem.*, 2025, 1–20.

33 X. Sun, *et al.*, Highly efficient adsorption and removal of phthalate esters by polymers of intrinsic microporosity, *J. Hazard. Mater.*, 2024, **480**, 136218.

34 A. Ali, *et al.*, Efficient removal of hexavalent chromium (Cr (VI)) from wastewater using amide-modified biochar, *Molecules*, 2023, **28**(13), 5146.

35 A. Ali, *et al.*, Efficient removal of Pb (II) from aqueous medium using chemically modified silica monolith, *Molecules*, 2021, **26**(22), 6885.

36 A. Ali, K. Saeed and F. Mabood, Removal of chromium (VI) from aqueous medium using chemically modified banana peels as efficient low-cost adsorbent, *Alex. Eng. J.*, 2016, **55**(3), 2933–2942.

37 A. Ali, Removal of Mn (II) from water using chemically modified banana peels as efficient adsorbent, *Environ. Nanotechnol. Monit. Manag.*, 2017, 7, 57–63.

38 A. Ali and K. Saeed, Decontamination of Cr (VI) and Mn (II) from aqueous media by untreated and chemically treated banana peel: a comparative study, *Desalination Water Treat.*, 2015, **53**(13), 3586–3591.

39 R. Cheraghi, *et al.*, Removal of Benzyl butyl phthalate by Polyetheretherketone/polyvinylalcohol nanocomposite Modified with Zinc oxide nanoparticles Adsorbent from Wastewater, *Pollution*, 2024, **10**(2), 833–846.

40 R. Yang, *et al.*, An effective method for the synthesis of yolk–shell magnetic mesoporous carbon-surface molecularly imprinted microspheres, *J. Mater. Chem. A*, 2016, **4**(25), 9807–9815.

41 X.-B. Yu, *et al.*, Preparation of trimethylchlorosilane-modified acid vermiculites for removing diethyl phthalate from water, *J. Colloid Interface Sci.*, 2012, **369**(1), 344–351.

42 X. Zhou, *et al.*, Adsorption of phthalic acid esters (PAEs) by amphiphilic polypropylene nonwoven from aqueous solution: the study of hydrophilic and hydrophobic microdomain, *J. Hazard. Mater.*, 2014, **273**, 61–69.

43 M. Farahmandjou and F. Soflaee, Synthesis and characterization of α-Fe2O3 nanoparticles by simple co-precipitation method, *Phys. Chem. Res.*, 2015, **3**(3), 191–196.

44 T. Bibi, *et al.*, Efficient removal of bisphenol A from water using C18 functionalized silica-coated iron oxide nanoparticles, *J. Nanopart. Res.*, 2025, **27**(1), 1–19.

45 Z. Ali, J.-P. Andreassen and S. Bandyopadhyay, Fine-Tuning of Particle Size and Morphology of Silica Coated Iron Oxide Nanoparticles, *Ind. Eng. Chem. Res.*, 2023, **62**(12), 4831–4839.

46 S. Alharthi, A. Ali and E. Y. Santali, Synthesis of chiral mesoporous silica nanoparticles for the adsorptive removal of the chiral insecticide sulfoxaflor from water, *Nanoscale Adv.*, 2025, 7, 1432–1442.

47 R. Dawn, *et al.*, Origin of magnetization in silica-coated Fe3O4 nanoparticles revealed by soft X-ray magnetic circular dichroism, *Braz. J. Phys.*, 2022, **52**(3), 99.

48 H. L. Ding, *et al.*, Fe3O4@SiO2 Core/Shell Nanoparticles: The Silica Coating Regulations with a Single Core for Different Core Sizes and Shell Thicknesses, *Chem. Mater.*, 2012, **24**(23), 4572–4580.

49 P. B. Shete, *et al.*, Water dispersible oleic acid-coated Fe3O4 nanoparticles for biomedical applications, *J. Magn. Magn. Mater.*, 2015, **377**, 406–410.

50 E. S. D. T. de Mendonça, *et al.*, Effects of silica coating on the magnetic properties of magnetite nanoparticles, *Surf. Interfaces*, 2019, **14**, 34–43.

51 M. M. Islam, *et al.*, Facile Fabrication and Characterization of Amine-Functional Silica Coated Magnetic Iron Oxide Nanoparticles for Aqueous Carbon Dioxide Adsorption, *ACS Omega*, 2024, **9**(19), 20891–20905.

52 A. Glaria, *et al.*, Silica coated iron nanoparticles: synthesis, interface control, magnetic and hyperthermia properties, *RSC Adv.*, 2018, **8**(56), 32146–32156.

53 H. Kohzadi and M. Soleiman-Beigi, XPS and structural studies of Fe3O4-PTMS-NAS@ Cu as a novel magnetic natural asphalt base network and recoverable nanocatalyst for the synthesis of biaryl compounds, *Sci. Rep.*, 2021, **11**(1), 24508.

54 L. Lu, J. Wang and B. Chen, Adsorption and desorption of phthalic acid esters on graphene oxide and reduced graphene oxide as affected by humic acid, *Environ. Pollut.*, 2018, **232**, 505–513.

55 T. Nawaz, *et al.*, Synthesis of diglycolic acid functionalized core-shell silica coated Fe3O4 nanomaterials for magnetic extraction of Pb (II) and Cr (VI) ions, *Sci. Rep.*, 2020, **10**(1), 10076.

56 A. S. I. A. Magid, *et al.*, Competitive adsorption of Dibutyl phthalate (DBP) and Di (2-ethylhexyl) phthalate (DEHP) onto fresh and oxidized corncob biochar, *Chemosphere*, 2021, **280**, 130639.

57 N. Orachorn, P. Klongklaew and O. Bunkoed, A composite of magnetic GOx@ MOF incorporated in alginate hydrogel

fiber adsorbent for the extraction of phthalate esters, *Microchem. J.*, 2021, **171**, 106827.

58 U. A. Qureshi, *et al.*, A comparative study and evaluation of magnetic and nonmagnetic hydrogels towards mitigation of di butyl and di ethyl hexyl phthalate from aqueous solutions, *J. Taiwan Inst. Chem. Eng.*, 2016, **59**, 578–589.

59 X. Diao, *et al.*, Preparation of 3, 3, 3-trifluoropropyl functionalized hydrophobic mesoporous silica and its outstanding adsorption properties for dibutyl phthalate, *RSC Adv.*, 2017, **7**(14), 8338–8346.

60 X. Wang, *et al.*, Adsorption of dibutyl phthalate in aqueous solution by mesoporous calcium silicate grafted non-woven polypropylene, *Chem. Eng. J.*, 2016, **306**, 452–459.

61 Q. Li, *et al.*, Fabrication of thermoresponsive metal–organic nanotube sponge and its application on the adsorption of endocrine-disrupting compounds and pharmaceuticals/ personal care products: Experiment and molecular simulation study, *Environ. Pollut.*, 2021, **273**, 116466.

62 H. Zhang, *et al.*, Enhanced adsorption of phthalic acid esters (PAEs) from aqueous solution by alkylbenzene-functionalized polypropylene nonwoven and its adsorption mechanism insight, *Chem. Eng. J.*, 2018, **331**, 406–415.

63 L. Gao, *et al.*, Preparation of Ti3C2Tx-based MXene composite aerogel and its adsorption performance for dibutyl phthalate, *Colloids Surf., A*, 2024, **686**, 133452.

64 Y. Yan, *et al.*, Tunable zirconium-based metal organic frameworks synthesis for dibutyl phthalate efficient removal: An investigation of adsorption mechanism on macro and micro scale, *J. Colloid Interface Sci.*, 2023, **650**, 222–235.

65 W. Xu, *et al.*, Synthesis of surface molecular imprinted polymers based on carboxyl-modified silica nanoparticles with the selective detection of dibutyl phthalate from tap water samples, *Appl. Surf. Sci.*, 2017, **426**, 1075–1083.